Low-cost high-efficiency system for solar-driven conversion of CO2 to hydrocarbons

Low-cost high-efficiency system for solar-driven conversion of CO_2 to hydrocarbons

Tran Ngoc Huan[a], Daniel Alves Dalla Corte[b], Sarah Lamaison[a], Dilan Karapinar[a], Lukas Lutz[b], Nicolas Menguy[c], Martin Foldyna[d], Silver-Hamill Turren-Cruz[e,f], Anders Hagfeldt[f], Federico Bella[g], Marc Fontecave[a,1], and Victor Mougel[a,1,2]

[a]Laboratoire de Chimie des Processus Biologiques, CNRS UMR 8229, Collège de France, Sorbonne Université, 75231 Paris Cedex 05, France; [b]Laboratoire de Chimie du Solide et Energie, FRE 3677 Collège de France, Sorbonne Université, 75231 Paris Cedex 05, France; [c]Sorbonne Université, UMR CNRS 7590, Muséum National d'Histoire Naturelle, Institut de Recherche pour le Développement, Institut de Minéralogie, de Physique des Matériaux et de Cosmochimie, 75005 Paris, France; [d]Laboratoire de Physique des Interfaces et des Couches Minces, CNRS, École Polytechnique, Université Paris–Saclay, 91128 Palaiseau, France; [e]Centro de Investigación en Dispositivos Semiconductores, Benemérita Universidad Autónoma de Puebla, CP 72570, Puebla, México; [f]Laboratory of Photomolecular Science, École Polytechnique Fédérale de Lausanne, 1015 Lausanne, Switzerland; and [g]Group for Applied Materials and Electrochemistry, Department of Applied Science and Technology, Politecnico di Torino, 10129 Torino, Italy

Edited by Richard Eisenberg, University of Rochester, Rochester, NY, and approved March 5, 2019 (received for review September 6, 2018)

Conversion of carbon dioxide into hydrocarbons using solar energy is an attractive strategy for storing such a renewable source of energy into the form of chemical energy (a fuel). This can be achieved in a system coupling a photovoltaic (PV) cell to an electrochemical cell (EC) for CO_2 reduction. To be beneficial and applicable, such a system should use low-cost and easily processable photovoltaic cells and display minimal energy losses associated with the catalysts at the anode and cathode and with the electrolyzer device. In this work, we have considered all of these parameters altogether to set up a reference PV–EC system for CO_2 reduction to hydrocarbons. By using the same original and efficient Cu-based catalysts at both electrodes of the electrolyzer, and by minimizing all possible energy losses associated with the electrolyzer device, we have achieved CO_2 reduction to ethylene and ethane with a 21% energy efficiency. Coupled with a state-of-the-art, low-cost perovskite photovoltaic minimodule, this system reaches a 2.3% solar-to-hydrocarbon efficiency, setting a benchmark for an inexpensive all–earth-abundant PV–EC system.

electrocatalysis | PV–EC | CO_2 reduction | electrolyzer | copper dendrites

The transformation of carbon dioxide is an energy-intensive process that must involve inexpensive sources of energy and high energy efficiency while maintaining the lowest possible cost. Artificial photosynthetic systems, which are technological devices that utilize sunlight as a source of energy and water as a source of electrons to convert CO_2 into energy-dense organic compounds (fuels or other carbon-based feedstocks for the chemical industry), are attractive in that context. This can be achieved using a photovoltaic (PV) cell to provide photogenerated electrons and holes to an electrochemical cell (EC) for water oxidation at the anode and CO_2 reduction at the cathode. Only a few examples of such PV–EC systems have been reported, predominantly leading to high CO or formate selectivity (1–3), and only two such systems have led to high hydrocarbons or alcohols selectivity (4, 5). Among them, the most efficient PV–EC systems have been based on costly components: A record 13% solar-to-CO conversion was achieved using a GaInP/GaInAs/Ge photovoltaic cell (3), while a 3% solar-to-hydrocarbon efficiency was reported with an iridium oxide anode coupled to a four-terminal III-V/Si tandem cell (5). Despite their unprecedented efficiency, these systems do not meet the critical requirement of using catalysts based only on earth-abundant elements and cost-efficient PV cells for large-scale use.

The design of a cheap and high-efficiency PV–EC system indeed requires an integrative approach that takes the four following aspects into account: (*i*) the development of robust CO_2 reduction (CO_2R) and oxygen evolution reaction (OER) electrocatalysts with low overpotentials and based on earth-abundant metals; (*ii*) their operation in moderate pH conditions, limiting corrosion issues and electrolyte consumption and allowing for long-term operation; (*iii*) their integration into an electrolyzer especially designed to maximize their efficiency and limit electrical energy losses; and (*iv*) the final coupling of the electrolyzer to a low-cost PV system. This approach might result in lower current densities than currently reported using catalysts operating in highly basic media (6–8). However, such current densities are sufficient to match the current densities provided by state-of-the-art perovskite PV cells (9).

Herein, we report an electrolyzer that uses the same copper-based catalyst at both the anode and cathode and achieves CO_2 reduction to hydrocarbons (ethylene and ethane) with a 21% energy efficiency. Subsequent coupling of this system to a state-of-the-art perovskite PV minimodule demonstrated a 2.3% solar-to-hydrocarbons efficiency, setting a benchmark for an inexpensive all–earth-abundant PV–EC system.

Results and Discussion

Maximizing the Energy Efficiency. The efficiency of a CO_2R/OER electrolyzer primarily depends on the activities of the catalysts,

Significance

Carbon dioxide electroreduction may constitute a key technology in coming years to valorize CO_2 as high value-added chemicals such as hydrocarbons and a way to store intermittent solar energy durably. Based on readily available technologies, systems combining a photovoltaic (PV) cell with an electrolyzer cell (EC) for CO_2 reduction to hydrocarbons are likely to constitute a key strategy for tackling this challenge. However, a low-cost, sustainable, and highly efficient PV–EC system has yet to be developed. In this article, we show that this goal can be reached using a low-cost and easily processable perovskite photovoltaic minimodule combined to an electrolyzer device using the same Cu-based catalysts at both electrodes and in which all energy losses have been minimized.

Author contributions: T.N.H., M. Fontecave, and V.M. designed research; T.N.H., D.A.D.C., S.L., D.K., L.L., S.-H.T.-C., F.B., and V.M. performed research; N.M., M. Foldyna, S.-H.T.-C., A.H., and F.B. contributed new reagents/analytic tools; T.N.H., D.A.D.C., N.M., A.H., F.B., M. Fontecave, and V.M. analyzed data; and T.N.H., M. Fontecave, and V.M. wrote the paper.

The authors declare no conflict of interest.

This article is a PNAS Direct Submission.

See Commentary on page 9693.

[1]To whom correspondence may be addressed. Email: marc.fontecave@college-de-france.fr or mougel@inorg.chem.ethz.ch.

[2]Present address: Department of Chemistry and Applied Biosciences, Eidgenössische Technische Hochschule Zürich, 8093 Zurich, Switzerland.

This article contains supporting information online at www.pnas.org/lookup/suppl/doi:10.1073/pnas.1815412116/-/DCSupplemental.

Published online March 27, 2019.

notably their ability to mediate both redox reactions with minimal overpotential losses. This is highly challenging as both anodic and cathodic reactions involve complex multielectron, multiproton reactions, especially when hydrocarbons are targeted. Furthermore, resistivity issues and membrane potential contributions can also significantly influence energy losses. The use of a single-compartment cell with anode and cathode in close proximity effectively solve membrane potential and resistivity-related issues (1, 4), but results in a gas mixture of the CO_2 reduction products and the anodically evolved oxygen. The lack of electrode separation, however, increases the chance of gas crossover that has a deleterious effect on the Faradaic yield (FY) for CO_2 reduction. Herein, we developed a two-compartment electrolyzer containing an anion-exchange membrane between the anodic and cathodic compartments. The overall cell potential can thus be expressed as the sum of the equilibrium potential, the kinetic overpotentials of CO_2R and OER, and the resistive and concentration losses (Eq. **1**):

$$E(J) = E_{rev} + E_{\Omega}(J) + \eta(J), \qquad [1]$$

$$E_{\text{rev}} = E^0{}_{\text{OER}} + E^0{}_{\text{CO2R}}; E_{\Omega}(J) = J \times \left(R_{\text{membrane}} + R_{\text{electrolyte}}\right) \times S_{\text{elect}}; \eta(J) = \eta_{\text{OER}}(J) - \eta_{\text{CO2R}}(J) + \eta_{\text{conc}}(J),$$

where E_{rev} is the reversible potential of the cell, E_{Ω} is the ohmic drop, and η is the cell overpotential. J is the current density at the cathode, and S_{elect} is the surface of the electrodes.

In this work, we take all of these parameters into consideration to develop a system with high selectivity toward hydrocarbons able to operate at currents over 25 $mA{\cdot}cm^{-2}$ and at a cell potential lower than 3 V, as low cell voltages are required for efficient coupling to photovoltaic cells.

Electrocatalysts. Thus far, copper is the only metal that has shown high selectivity for CO_2R to multicarbon products, particularly when prepared by reduction of CuO materials (10–12). In addition, we and others have demonstrated that CuO can function as an efficient OER catalyst at the moderate pH conditions required for efficient CO_2R (13–16). Consequently, we selected a copper oxide-based catalyst for both anode and cathode material. This strategy presents the additional advantage of limiting the poisoning of the cathode by redepositing the metal used for the anode (3). This phenomenon has been previously observed in the context of CO_2 reduction when using earth-abundant OER catalysts, and shown to result in a decrease of selectivity for CO_2 reduction over time (1).

Aiming at lowering mass transport losses (η_{conc}), we selected a dendritic nanostructured copper oxide material (DN-CuO) that we recently reported as highly efficient and stable OER catalyst (13). This material presents both a macroporous structure, provided by cavities larger than 50 μm, and a mesoporous structure resulting from the dendritic structure constituting the walls (*SI Appendix*, Fig. S1). This unique morphology ensures an efficient mass transfer of reactants and products while preserving a high electrochemical surface area.

Electrolyzer. The design of the electrolyzer has a profound influence on the overall CO_2 reduction performance, as it not only affects the cell voltage but also the selectivity of CO_2R, the product separation, and the catalyst stability (17, 18). To reach the highest overall efficiency, we target minimizing both ohmic and mass transport losses (Eq. **1**).

The most straightforward way to reduce the overall cell resistance is to lower the interelectrode distance and to use a concentrated electrolyte solution. However, such an approach faces two main limitations: (*i*) in a CO_2-saturated solution, a thin cathodic compartment favors formation and trapping of gas bubbles, thus strongly increasing the resistance of the cell, and (*ii*) a concentrated bicarbonate solution increases the catalytic selectivity for proton reduction at the expense of CO_2 reduction, as shown here and in previous reports (4, 19, 20). Optimal results were obtained using a 7-mm interelectrode distance and a 0.1 M cesium bicarbonate ($CsHCO_3$) CO_2-saturated (pH 6.8) solution as the cathodic electrolyte combined with a 0.2 M cesium carbonate (Cs_2CO_3) solution (pH 11) as the anodic electrolyte. We showed that larger concentrations of the electrolytes, while decreasing the overall cell resistivity, lowered faradaic efficiency for CO_2 reduction (*SI Appendix*, Fig. S18). Similarly, we observed that using other alkali-metal cations resulted in an overall decrease in current for the same applied potential (*SI Appendix*, Fig. S19). Multiple reports have shown the beneficial influence of large alkali cations on both the selectivity for multicarbon products in CO_2 reduction and on lowering the overpotential for water oxidation (21, 22). Using HCO_3^- as the charge carrier for both the anodic and cathodic compartments together with an anion exchange membrane (AEM) allows for continuous operation of the system at high current densities: continuous CO_2 bubbling in the catholyte regenerates the diffused bicarbonate anions. In addition, the moderate pH difference between the anodic and cathodic compartment allows a minimal contribution of the pH gradient to the membrane potential.

One of the key factors lowering the efficiency of CO_2 conversion is mass transfer of CO_2 to the cathode surface. This is especially true in aqueous solution because of the low solubility of CO_2. To overcome this limitation, we used a continuous-flow electrochemical cell in which the anolyte and catholyte are continuously flowed through the system. Constant saturation in CO_2 is ensured by continuously purging the catholyte with CO_2 in a separate compartment, which additionally continuously evacuates the reaction products. A schematic representation of the electrolyzer cell used here is given in *SI Appendix*, Figs. S2 and S3.

Electrocatalytic Performances. Linear sweep voltammetry (LSV) was carried out at 10 $mV{\cdot}s^{-1}$ to evaluate the electrocatalytic activity of the DN-CuO electrodes for both CO_2 reduction and water oxidation using this setup (Fig. 1*A*). The low cathodic onset potential of −0.3 V vs. reversible hydrogen electrode (RHE) and the high current densities (up to 25 $mA{\cdot}cm^{-2}$ at −0.95 V vs. RHE) illustrates the excellent CO_2R electrocatalytic activity of DN-CuO, reported here. The anodic catalytic wave shows a similar onset potential for water oxidation as reported in our previous work (13), but accompanied with an increased current density, illustrating the beneficial influence of the electrolyzer system on the catalytic performance. The *J*–*E* curve of the electrolyzer cell (Fig. 1*B*) shows that a current density of 25 $mA{\cdot}cm^{-2}$ can be obtained at a cell potential below 3 V, a consequence of the low resistivity of the electrolyzer. The different contributions to the overall cell potential are detailed in *SI Appendix*, Fig. S4, presenting the equivalent circuit diagram of the electrolyzer cell.

Controlled-potential electrolysis was carried out for 1 h at various fixed cathode potentials (*SI Appendix*, Fig. S5). Identification and quantification of the gas-phase products from the cathodic compartment were achieved by on-line GC, while the liquid-phase products were analyzed by ion-exchange chromatography and NMR spectroscopy. Significant amounts of ethylene (C_2H_4) and ethane (C_2H_6) were obtained at applied potentials below −0.8 V vs. RHE (Fig. 1*C*). The highest selectivity for CO_2 reduction (vs. H_2 formation) and hydrocarbon production (vs. CO and HCOOH formation) was obtained at a cathode potential of −0.95 V vs. RHE (Fig. 1*C* and *SI Appendix*, Fig. S6). This corresponds to a cell potential of 2.95 V, at which a stable current density of 25 $mA{\cdot}cm^{-2}$ was obtained during 3-h electrolysis (*SI Appendix*, Fig. S7). In these conditions, CO_2 reduction products accounted for a 62% FY, without loss of selectivity over the course of the electrolysis. Among the CO_2

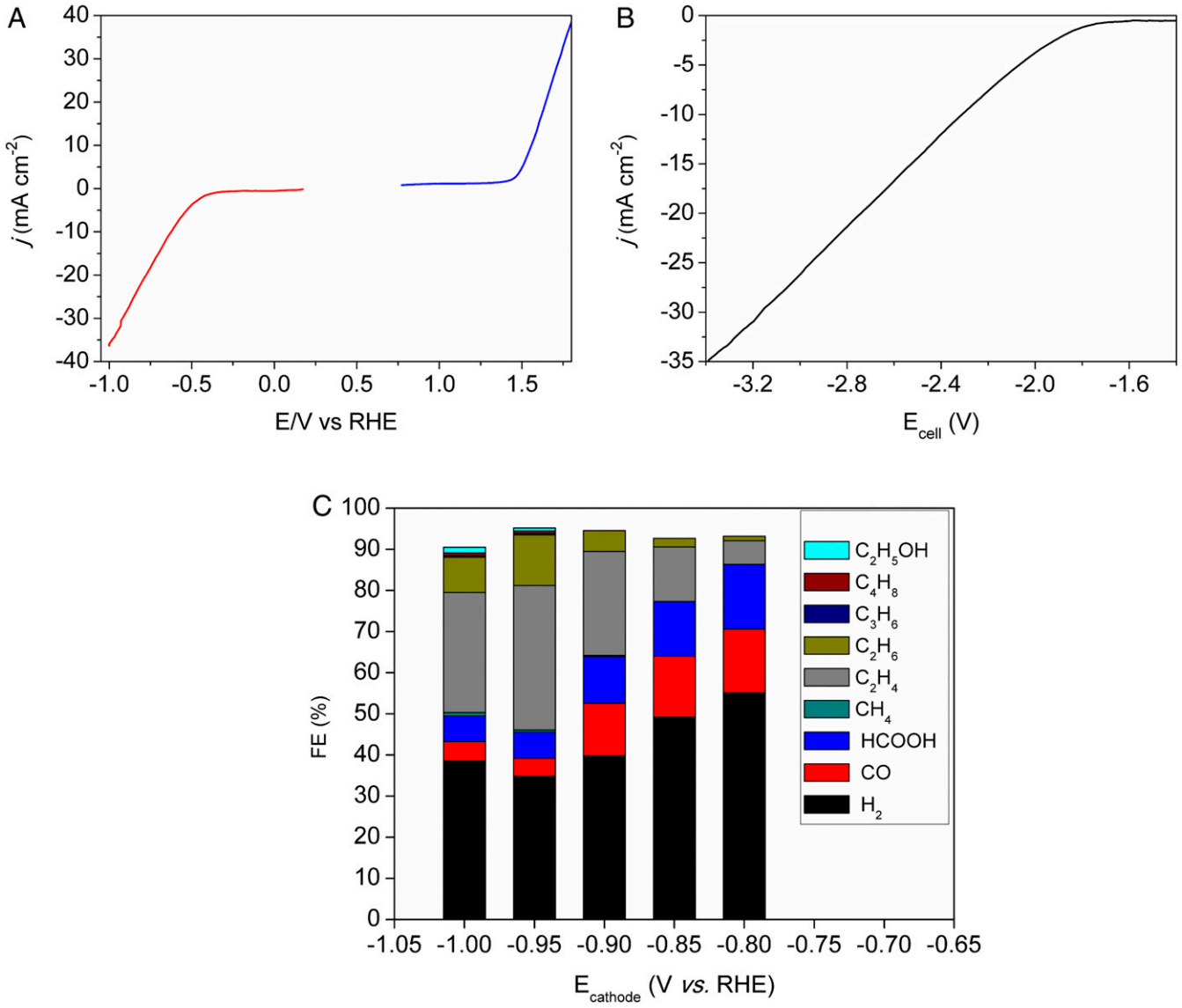

Fig. 1. (*A*) LSV of 1-cm^2 DN-CuO cathode (red) and anode **1** (blue), using a scan rate of 10 mV·s^{-1} (currents are uncorrected for resistive losses incurred within the electrolyte; all current densities are based on projected geometric area). (*B*) *J–E* curve of the electrolyzer cell using 1-cm^2 DN-CuO electrodes. (*C*) Faradaic yields (FYs) for CO_2 reduction products using 1-cm^2 DN-CuO cathode at different potentials. All measurements were carried out using the electrolyzer cell described in the main text and *SI Appendix*, Fig. S2 using an AEM separating the cathodic (CO_2-saturated 0.1 M $CsHCO_3$) and anodic (0.2 M Cs_2CO_3) compartments. Constant CO_2 saturation was ensured by continuous sparging of the cathodic electrolyte with CO_2 at 2.5 mL·min^{-1}. FY values are detailed in *SI Appendix*, Table S1, and error bars are provided in *SI Appendix*, Fig. S8. E_{cell} is the electrolyzer cell potential, and $E_{cathode}$ is the applied cathode potential.

reduction products, C_2H_4 accounted for 57% (37% FY), C_2H_6 for 18% (12.8% FY), HCOOH for 11% (7% FY), and CO for 8% (5% FY) (partial currents for the different products are given in *SI Appendix*, Fig. S8). This high selectivity and production rate for hydrocarbons at such a low cell potential is unprecedented (4, 5) and corresponds to a record cell energy efficiency for hydrocarbons of 21% (calculated using the thermoneutral potential of C_2H_4 and C_2H_6; see *SI Appendix*, Table S2, for details). ^{13}C-labeling experiments confirmed CO_2 as the sole source of carbon for all carbon-containing products (*SI Appendix*, Fig. S9).

To illustrate the advantages of using a continuous-flow electrolyzer cell, we tested the DN-CuO electrodes within a standard H-type electrochemical cell in which CO_2 was continuously bubbled through the cathodic compartment, using the same electrolytes and anion-exchange membrane. The current density–voltage characteristic of this cell, displayed in *SI Appendix*, Fig. S10, indicates that while the overall onset potential for the electrolyzer is identical, the efficiency of the standard H-type electrolyzer is much lower than that of the electrolyzer cell developed in this work. This is clearly illustrated by the difference in cell potential required to obtain a stable current of 25 mA·cm^{-2}; 4.8 V were needed in the H-type electrolyzer, which produced hydrocarbons with a 6% energy efficiency, compared with 2.95 V in the continuous-flow electrochemical cell developed here, which led to the aforementioned 21% energy efficiency for hydrocarbon production (see *SI Appendix* for details).

Postcharacterization of the Cathode. The characterization of DN-CuO has been reported previously (13). It consists of a triple-layer structure with a metallic copper core covered by successive layers of Cu_2O (~200-nm thickness) and CuO (~50-nm thickness) (Figs. 2 and 3*A*), both layers contributing to the good catalytic activity of the material (13). We characterized the DN-CuO cathode

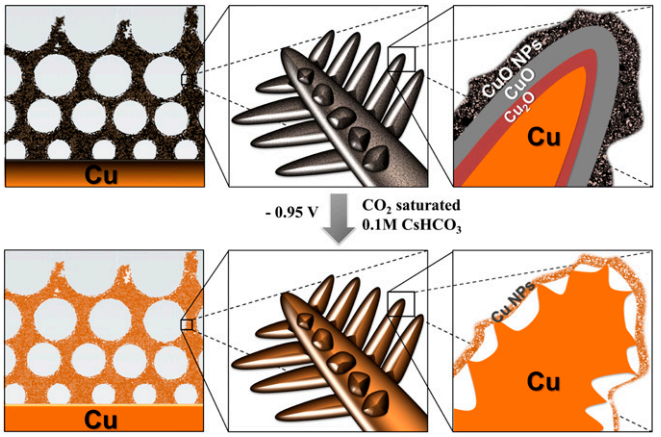

Fig. 2. Schematic view of the DN-CuO before (*Top*) and after (*Bottom*) CO_2 electroreduction in 0.1 M $CsHCO_3$.

after 1-h electrolysis at −0.95 V vs. RHE in the optimized CO_2 reduction conditions described above. Scanning electron microscopy (SEM) images (*SI Appendix*, Fig. S1) showed no significant change in the morphology of the electrode. To gain more insight on structural changes occurring upon reduction, scanning transmission electron microscopy (STEM) images, selected area electron diffraction (SAED) analysis, and elemental mapping of focused ion beam (FIB) cross-sections of the DN-CuO before and after electrolysis as a cathode were recorded (Figs. 2 and 3 *C–F* and *SI Appendix*, Fig. S11). Both SAED patterns and elemental mapping images show that copper oxide was reduced to metallic copper under CO_2 reduction conditions (*SI Appendix*, Fig. S11). Interestingly, the STEM images shows that during reduction the shape of the nanostructure and the external morphology of the electrode were retained while a thin outer layer of Cu nanoparticles appeared at the electrode surface, the internal structure revealing Kirkendall voids (Fig. 3 *C* and *E*) (23). The increased porosity of the electrode is confirmed by a slight increase in electrochemical surface area (23.1 cm^2 after electrolysis vs. 20.6 cm^2 before electrolysis). The nanostructuration of the material plays a critical role regarding its selectivity, as witnessed by the comparison with the parent crystalline Cu dendrites (13), showing <10% FY for ethylene at −0.95 V vs. RHE (*SI Appendix*, Fig. S12). Such a beneficial influence of cavities in Cu electrocatalysts for multicarbon products was recently demonstrated in the context of carbon monoxide electroreduction (24). This specific nanostructure does not change over prolonged electrolysis, as witnessed by the STEM characterization of FIB slices of the electrode after 3-h operation (*SI Appendix*, Fig. S13). Furthermore, only trace amounts of Cu (<0.02% of total electrodeposited Cu on DN-CuO cathode) were released in the electrolyte solution over 3-h electrolysis, as revealed by inductively coupled plasma (ICP) analysis (*SI Appendix*).

PV–EC Coupling. A PV–EC system has the advantage of relying on mature technologies benefiting from advanced experience of the industry innovations and continuously decreasing costs (25). However, while the separation of light capture and catalysis within two different devices allows for independent optimization and better control of the performances and scalability, correct matching of the PV power output to the number and sizing of EC cells is challenging. When a solar cell and an electrolyzer are directly connected, the electrical circuit requires the operating current and voltage to be the same for the two devices, and their values are determined by the crossing point between the current–voltage curves for the two devices. More specifically, to reach the highest efficiency: (*i*) the operating point (current, voltage) of the device must be as close as possible to the maximum power point for solar-to-electric energy conversion, and (*ii*) this working cell potential must correspond to the potential at which the highest selectivity for the products of interest, in this case hydrocarbons, is obtained.

In this study, we used triple cation perovskite solar cells stabilized with a photocured coating (26). The typical current–voltage characteristic of a single PV cell (0.25 cm^2) under 1 sun (AM 1.5G; 100 $mW{\cdot}cm^{-2}$) is shown in *SI Appendix*, Fig. S14. It shows a short-circuit photocurrent of 6.8 mA and a solar-to-electrical energy conversion ($\eta_{S\text{-}E}$) of 18.5%. To provide a PV voltage and current density compatible with the electrolyzer conditions required for the most selective transformation of CO_2 to hydrocarbons, we built a minimodule constituted by two series of three perovskite solar cells connected in parallel (*SI Appendix*, Fig. S15). The photovoltaic current–voltage characteristic of this minimodule is presented in Fig. 4*A* (black squares), which shows a maximum $\eta_{S\text{-}E}$ of 17.5% at 10.0 mA and 2.45 V (*SI Appendix*, Fig. S16), slightly decreased with respect to a single module. On the basis of the polarization curves presented in Fig. 1, the geometric surface areas of the cathode and the anode were adjusted to 0.35 and 0.85 cm^2, respectively, for optimal match between the current–voltage characteristics of the electrolyzer cell

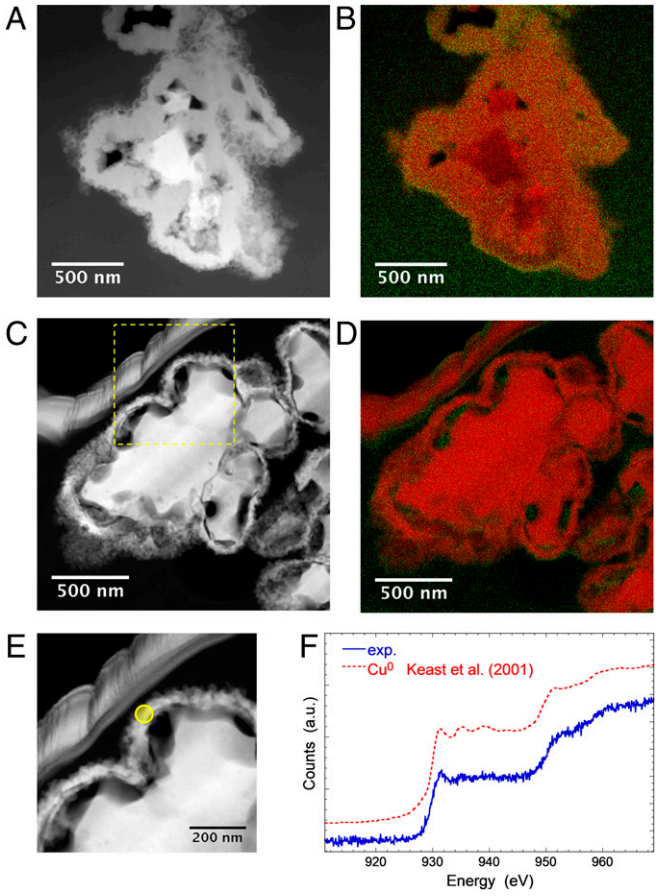

Fig. 3. STEM–high-angle annular dark-field analysis of FIB cross-sections of DN-CuO before (*A* and *B*) and after (*C–E*) 1-h electroreduction of CO_2 at −1.0 V vs. RHE in CO_2-saturated 0.1 M $CsHCO_3$. (*B–D*) STEM–energy-dispersive X-ray spectroscopy analyses (Cu in red, O in green). (*E* and *F*) Electron energy loss spectroscopy analysis of the axis indicated in *E*, identifying Cu^0 as the main oxidation state (28) at the surface of the electrode after 1-h electroreduction of CO_2 at −1.0 V vs. RHE in CO_2-saturated 0.1 M $CsHCO_3$.

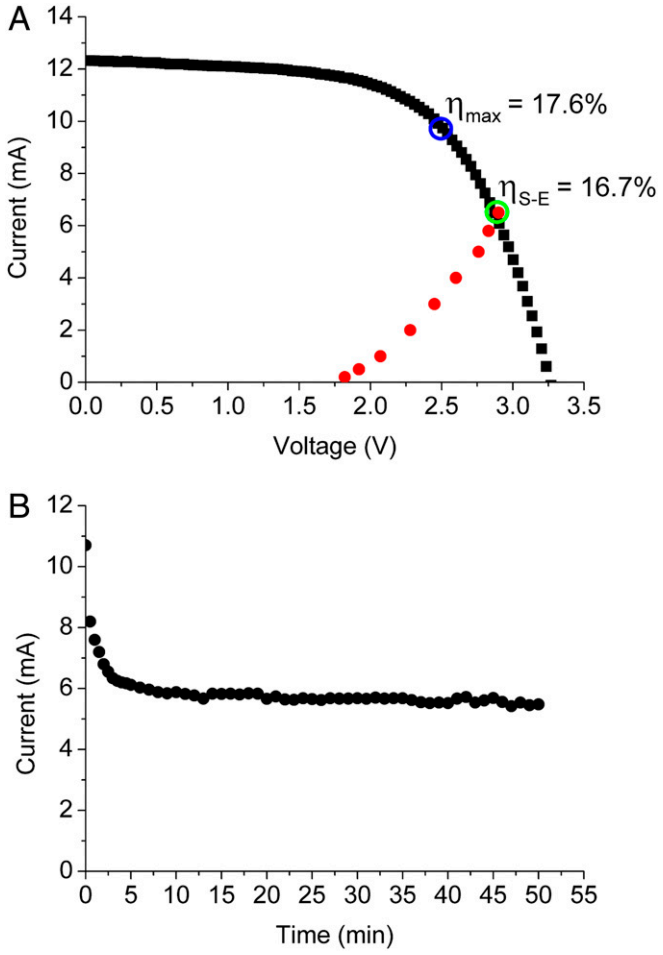

Fig. 4. (*A*) Current–potential characteristic of the perovskite minimodule under 1 sun, AM 1.5G illumination (black squares) and measured operating current of the electrolyzer cell (geometric areas of cathode, 0.35 cm^2, and anode, 0.85 cm^2; current measured after 5-min electrolysis) at various potentials (red dots). (*B*) Electrolyzer cell current as a function of photoelectrolysis time using the perovskite minimodule as the sole energy source.

and of the minimodule. The measured operating current of the electrolyzer cell at various potentials is shown in Fig. 4*A*, the theoretical operating point of the PV–EC system being given by the intersection with the PV current–voltage characteristic. With this setup, stable currents were obtained and high selectivity for C_2 hydrocarbons was preserved over more than 6-h operation time (*SI Appendix*, Fig. S17). When both systems were connected, without external bias and under a constant AM 1.5G illumination, a stable current of 6.0 ± 0.2 mA (corresponding to a current density of ~18 $mA{\cdot}cm^{-2}$ at the cathode) and a potential of 2.8 ± 0.02 (V) were recorded at the electrolyzer terminals. The system showed a stable current over 50-min electrolysis (Fig. 4*B*), during which time CO_2R products were continuously analyzed by on-line GC. Selectivity did not vary during the run, C_2H_4 and C_2H_6 being obtained as the main products with an average FY of 40.5% (34% for C_2H_4 and 6.5% for C_2H_6), together with CO and HCOOH in 4.8% and 6.4% FY, respectively. Concomitant hydrogen production was observed with 42.2% FY. The lower selectivity of the electrolyzer using smaller electrodes can be explained by the slightly more negative potential of the cathode when a smaller cathode size is used. These measured current densities and FY allowed determining a solar-to-hydrocarbon (ethylene and ethane) efficiency of 2.3% (*SI Appendix*). This high efficiency constitutes a benchmark for solar-to-hydrocarbon products when using easily processable perovskite PV cells and earth-abundant metal catalysts (see *SI Appendix*, Table S2 for comparison with other PV–EC systems).

Conclusions

In this work, we have elaborated an artificial photosynthetic system based on nonnoble metals and inexpensive material exclusively able to convert CO_2 to hydrocarbons with a benchmark solar-to-hydrocarbon efficiency of 2.3%. This could be achieved through (*i*) the demonstration that a dendritic nanostructured copper oxide material behaves as a highly efficient electrocatalyst for both OER and CO_2R and can be used both at the anode and the cathode, thus allowing to reduce production cost and issues related to metal contaminant deposit at the cathode during operation; (*ii*) a thorough consideration of all of the possible losses in the electrolyzer system resulting from hardware and catalysts issues, which allowed designing a tailor-made electrolyzer for overall CO_2 reduction to hydrocarbons with a 21% energy efficiency.

Materials and Methods

Additional details regarding the materials and methods may be found in *SI Appendix*.

General Considerations. Electrocatalytic measurements and electrolysis experiments were carried out using a Bio-logic SP300 potentiostat.

Photovoltaic characterization was carried out by using solar simulator system, Newport's Oriel Sol3A class AAA solar simulator (model 94083A) with certified 8″ × 8″ homogeneity under 1-sun illumination.

H_2 and gaseous CO_2 reduction products were analyzed by GC (Multi-Gas Analyzer #5; SRI Instruments), equipped with Haysep D and MoleSieve 5A columns and thermal conductivity detector and flame ionization detector with methanizer using argon as a carrier gas. GC was calibrated by using a standard gas mixture containing 2,500 ppm of H_2, CO, CH_4, C_2H_4, C_2H_6, C_3H_6, C_3H_8, C_4H_8, and C_4H_{10} in CO_2 (Messer). The liquid-phase products were quantified using ionic exchange chromatography (formate and oxalate; 883 Basic IC; Metrohm) and NMR spectroscopy (Bruker AVANCE III 300 spectrometer). Fourier-transform infrared spectroscopy measurements were carried out using a SHIMADZU IR Affinity-1S spectrometer.

SEM images were acquired using a Hitachi S-4800 scanning electron microscope. Transmission electron microscopy images were obtained on a JEM-2010F transmission electron microscope (JEOL) with an accelerating voltage of 200 kV.

$CuSO_4{\cdot}5H_2O$ (99.9%), H_2SO_4 (99.8%), $CsHCO_3$ (99.8%), Cs_2CO_3 (99.9%), and ^{13}C-labeled CO_2 (99 atom % ^{13}C, <3 atom % ^{18}O) were purchased from Sigma-Aldrich as used without further purification. DN-CuO electrodes and Cu dendrites were prepared according to previously reported procedure (13).

Cu content in the electrolyte solutions was determined by ICP-AES analysis using a Thermo Fisher iCAP 6000 device instrument.

Solar Cells Preparation.

Substrate preparation and Li-doping TiO_2. Nippon Sheet Glass 10 Ω/sq was cleaned by sonication in 2% Hellmanex water solution for 30 min. After rinsing with deionized water and ethanol, the substrates were further cleaned with UV ozone treatment for 15 min. Then, a 30-nm-thick TiO_2 compact layer was deposited on FTO via spray pyrolysis at 450 °C from a precursor solution of titanium diisopropoxide bis(acetylacetonate) in anhydrous ethanol. After the spraying, the substrates were left at 450 °C for 45 min and left to cool down to room temperature. Then, a mesoporous TiO_2 layer was deposited by spin coating (SPIN150i model, s/n R050962, SPS-Europe GmbH) for 20 s at 4,000 rpm with a ramp of 2,000 $rpm{\cdot}s^{-1}$, using 30-nm particle paste (Dyesol 30 NR-D) diluted in ethanol to achieve 150- to 200-nm-thick layer. After spin coating, the substrates were immediately dried at 100 °C for 10 min and then sintered again at 450 °C for 30 min under dry airflow.

Li-doping of mesoporous TiO_2 was accomplished by spin coating a 0.1 M solution of Li-TFSI in acetonitrile at 3,000 rpm for 30 s followed by another sintering step at 450 °C for 30 min. After cooling down to 150 °C, the substrates were immediately transferred in a nitrogen atmosphere glove box for depositing the perovskite films.

Perovskite precursor solution. Perovskite solutions were prepared by using the organic cation iodide salts (Dyesol), lead compounds (TCI), and RBI (abcr GmbH) as follows. First, the mixed cation precursor solution was prepared with FAI (1 M), PbI_2 (1.1 M), MABr (0.2 M), and $PbBr_2$ (0.22 M) in anhydrous DMF:DMSO 4:1 (vol/vol). To achieve a triple cation composition, CsI (1.5 M) in

DMSO was added to the mixed perovskite (MA/FA) precursor solution in a volume ratio of 5:95. To reach the final quadruple composition, RbI (1.5 M) in DMF:DMSO 4:1 (vol/vol) was added to the Cs/FA/MA triple cation perovskite in a volume ratio of 5:95 (27).

Perovskite deposition. The perovskite solution were spin coated in a two-step program at 1,000 and 4,000 rpm for 10 and 30 s, respectively. During the second step, 200 μL of chlorobenzene was poured on the spinning substrate 20 s before the end of the program. The substrates were then annealed (at 100 °C, unless stated otherwise) for 1 h in a nitrogen-filled glove box.

Hole transporting layers. After the perovskite annealing, the substrates were cooled down for a few minutes, and a spiro-OMeTAD (Merck) solution (70 mM in chlorobenzene) was spin-coated at 4,000 rpm for 20 s. Spiro-OMeTAD was doped with bis(trifluoromethylsulfonyl)imide lithium salt (Li-TFSI) (Sigma-Aldrich), tris(2-(1*H*-pyrazol-1-yl)-4-*tert*-butylpyridine)-cobalt(III) tris(bis(trifluoromethylsulfonyl)imide) (FK209) (Dynamo), and 4-*tert*-butylpyridine (tBP) (Sigma-Aldrich). The molar ratios of additives for spiro-OMeTAD were 0.5, 0.03, and 3.3 for Li-TFSI, FK209, and tBP, respectively. Finally, 80 nm of gold top electrode were thermally evaporated under high vacuum.

Perovskite solar cells were then stabilized with a photopolymerized coating accordingly to previously reported procedure (26).

Flow Electrochemical Cell. The scheme of the flow electrochemical cell is presented in *SI Appendix*, Fig. S2. The distance between cathode and anode is 0.7 cm approximately. The cathode and anode compartment are separated by a Selemion AEM. The geometrical surface area of the working electrodes was chosen to 1 cm^2 in all of this study, unless otherwise specified. Ag wire was used as the reference electrode and placed in both compartments, and was calibrated with an aqueous Ag/AgCl reference electrode before each experiment. The electrode potentials were referred to RHE according to the following formula:

$$E(\text{vs. RHE}) = E(\text{vs. Ag wire}) + \Delta E + 0.2 + 0.059 \times \text{pH}.$$

The potential difference (ΔE) between the Ag wire and the Ag/AgCl electrode was determined using the $E_{1/2}$ potential of $K_3Fe(CN)_6$ in 0.1 M $CsHCO_3$ solution as a reference. Unless otherwise stated, catalytic activity was investigated in this setup using CO_2-saturated 0.1 M $CsHCO_3$ (pH 6.8) at the cathode and 0.2 M Cs_2CO_3 (pH 11.0) at the anode, flowed through the two compartments at a constant flow of 1.0 mL·min^{-1}. Constant CO_2 saturation of the catholyte was ensured by continuous sparging with CO_2 at 2.5 mL·min^{-1}.

ACKNOWLEDGMENTS. We acknowledge Dr. David Troadec and the French RENATECH Network for the preparation of FIB cross-sections and Domitille Giaume for her help with ICP-MS analyses. We thank Sphere Energy (https://www.sphere-energy.eu/) for the realization of the electrolyzer cell. F.B. thanks Politecnico di Torino and Compagnia di San Paolo for the financial support through the call "Metti in rete la tua idea di ricerca" (PEPPY project). V.M. acknowledges financial support from CNRS–Cellule Energie and Fondation of College de France for the acquisition of the flow electrochemical system.

1. Schreier M, et al. (2015) Efficient photosynthesis of carbon monoxide from CO_2 using perovskite photovoltaics. *Nat Commun* 6:7326.
2. White JL, Herb JT, Kaczur JJ, Majsztrik PW, Bocarsly AB (2014) Photons to formate: Efficient electrochemical solar energy conversion via reduction of carbon dioxide. *J CO_2 Util* 7:1–5.
3. Schreier M, et al. (2017) Solar conversion of CO_2 to CO using Earth-abundant electrocatalysts prepared by atomic layer modification of CuO. *Nat Energy* 2:17087.
4. Ren D, Loo NWX, Gong L, Yeo BS (2017) Continuous production of ethylene from carbon dioxide and water using intermittent sunlight. *ACS Sustain Chem Eng* 5: 9191–9199.
5. Gurudayal, et al. (2017) Efficient solar-driven electrochemical CO_2 reduction to hydrocarbons and oxygenates. *Energy Environ Sci* 10:2222–2230.
6. Ma S, et al. (2016) One-step electrosynthesis of ethylene and ethanol from CO_2 in an alkaline electrolyzer. *J Power Sources* 301:219–228.
7. Dinh C-T, et al. (2018) CO_2 electroreduction to ethylene via hydroxide-mediated copper catalysis at an abrupt interface. *Science* 360:783–787.
8. Gabardo CM, et al. (2018) Combined high alkalinity and pressurization enable efficient CO_2 electroreduction to CO. *Energy Environ Sci* 11:2531–2539.
9. Correa-Baena J-P, et al. (2017) The rapid evolution of highly efficient perovskite solar cells. *Energy Environ Sci* 10:710–727.
10. Dutta A, Rahaman M, Mohos M, Zanetti A, Broekmann P (2017) Electrochemical CO_2 conversion using skeleton (sponge) type of Cu catalysts. *ACS Catal* 7:5431–5437.
11. Lum Y, Yue B, Lobaccaro P, Bell AT, Ager JW (2017) Optimizing C–C coupling on oxide-derived copper catalysts for electrochemical CO_2 reduction. *J Phys Chem C* 121: 14191–14203.
12. Mistry H, et al. (2016) Highly selective plasma-activated copper catalysts for carbon dioxide reduction to ethylene. *Nat Commun* 7:12123.
13. Huan TN, et al. (2017) Nanostructured oxygen-evolving copper oxide electrocatalyst. *Angew Chem Int Ed* 56:4792–4796.
14. Joya KS, de Groot HJM (2016) Controlled surface-assembly of nanoscale leaf-type Cu-oxide electrocatalyst for high activity water oxidation. *ACS Catal* 6:1768–1771.
15. Liu X, et al. (2016) Self-supported copper oxide electrocatalyst for water oxidation at low overpotential and confirmation of its robustness by Cu K-edge X-ray absorption spectroscopy. *J Phys Chem C* 120:831–840.
16. Yu F, Li F, Zhang B, Li H, Sun L (2015) Efficient electrocatalytic water oxidation by a copper oxide thin film in borate buffer. *ACS Catal* 5:627–630.
17. Yang W, Dastafkan K, Jia C, Zhao C (2018) Design of electrocatalysts and electrochemical cells for carbon dioxide reduction reactions. *Adv Mater Technol* 3:1700377.
18. Weekes DM, Salvatore DA, Reyes A, Huang A, Berlinguette CP (2018) Electrolytic CO_2 reduction in a flow cell. *Acc Chem Res* 51:910–918.
19. Wuttig A, Yaguchi M, Motobayashi K, Osawa M, Surendranath Y (2016) Inhibited proton transfer enhances Au-catalyzed CO_2-to-fuels selectivity. *Proc Natl Acad Sci USA* 113:E4585–E4593.
20. Huan TN, et al. (2017) Electrochemical reduction of CO_2 catalyzed by Fe-N-C materials: A structure–selectivity study. *ACS Catal* 7:1520–1525.
21. Kang Q, et al. (2017) Effect of interlayer spacing on the activity of layered manganese oxide bilayer catalysts for the oxygen evolution reaction. *J Am Chem Soc* 139: 1863–1870.
22. Zhu L, Du J, Zuo S, Chen Z (2016) Cs(I) cation enhanced Cu(II) catalysis of water oxidation. *Inorg Chem* 55:7135–7140.
23. Fan HJ, Gösele U, Zacharias M (2007) Formation of nanotubes and hollow nanoparticles based on Kirkendall and diffusion processes: A review. *Small* 3:1660–1671.
24. Zhuang T-T, et al. (2018) Copper nanocavities confine intermediates for efficient electrosynthesis of C3 alcohol fuels from carbon monoxide. *Nat Catal* 1:946–951.
25. McKone JR, et al. (2016) Translational science for energy and beyond. *Inorg Chem* 55: 9131–9143.
26. Bella F, et al. (2016) Improving efficiency and stability of perovskite solar cells with photocurable fluoropolymers. *Science* 354:203–206.
27. Saliba M, et al. (2016) Incorporation of rubidium cations into perovskite solar cells improves photovoltaic performance. *Science* 354:206–209.
28. Keast VJ, Scott AJ, Brydson R, Williams DB, Bruley J (2001) Electron energy-loss near-edge structure—a tool for the investigation of electronic structure on the nanometre scale. *J Microsc* 203:135–175.